

LA-UR-24-32101

Accepted Manuscript

Overview of oxygen opacity experiments at the national ignition facility and investigation of potential systematic errors

Mayes, D. C.; Hobbs, B. A.; Heeter, R. F.; Perry, Theodore Sonne; Johns, Heather Marie; Opachich, Y. P.; Hohenberger, M.; Bradley, Paul Andrew; Dutra, E. C.; Fontes, Christopher John; Gallardo-Diaz, E.; Montgomery, M. H.; Robey, Harry F. III; Wallace, M. S.; Winget, D. E.

Provided by the author(s) and the Los Alamos National Laboratory (1930-01-01).

To be published in: High Energy Density Physics

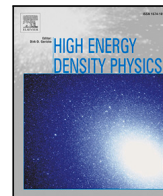
DOI to publisher's version: 10.1016/j.hedp.2025.101177

Permalink to record:

<https://permalink.lanl.gov/object/view?what=info:lanl-repo/lareport/LA-UR-24-32101>




Los Alamos National Laboratory, an affirmative action/equal opportunity employer, is operated by Triad National Security, LLC for the National Nuclear Security Administration of U.S. Department of Energy under contract 89233218CNA000001. By approving this article, the publisher recognizes that the U.S. Government retains nonexclusive, royalty-free license to publish or reproduce the published form of this contribution, or to allow others to do so, for U.S. Government purposes. Los Alamos National Laboratory requests that the publisher identify this article as work performed under the auspices of the U.S. Department of Energy. Los Alamos National Laboratory strongly supports academic freedom and a researcher's right to publish; as an institution, however, the Laboratory does not endorse the viewpoint of a publication or guarantee its technical correctness.



Research paper

Overview of oxygen opacity experiments at the national ignition facility and investigation of potential systematic errors

D.C. Mayes^a ,* B.A. Hobbs^a, R.F. Heeter^b, T.S. Perry^c, H.M. Johns^c, Y.P. Opachich^b, M. Hohenberger^b, P.A. Bradley^c, E.C. Dutra^d, C.J. Fontes^c, E. Gallardo-Diaz^e, M.H. Montgomery^a, H.F. Robey^c, M.S. Wallace^d, D.E. Winget^a

^a University of Texas at Austin, Austin, TX, 78712, USA

^b Lawrence Livermore National Laboratory, Livermore, CA, 94550, USA

^c Los Alamos National Laboratory, Los Alamos, NM, 87545, USA

^d Nevada National Security Site, Livermore Operations, Livermore, CA, 94550, USA

^e University of Nevada, Reno, Reno, NV, 89557, USA

ARTICLE INFO

Keywords:

Stellar interior

Opacity

Oxygen

ABSTRACT

Experiments to measure oxygen opacity at stellar interior conditions have been performed at the National Ignition Facility in a Discovery Science campaign. These experiments utilize the Opacity-on-NIF platform with a sample comprised of O, Mg, and Si. The spectral data from the Opacity Spectrometer cover the 1000–2000 eV photon energy range showing bound-free continuum absorption from O and line absorption from Mg and Si. DANTE and the Gated X-ray Detector are employed to measure the sample plasma's temperature and density, respectively. Initial data show lower transmission than expected by theoretical models, raising questions of whether potential background or data uniformity concerns could produce systematic errors in the inferred transmission. Here, we investigate three concerns thought to be important for the oxygen opacity data, including instrumental scattered background, sample self-emission non-uniformity, and backlight continuum non-uniformity. Additionally, we show the effect of a recently developed method to account for 2nd order crystal reflection. The total effect of these concerns on one experiment is found to be small compared to the observed difference between the inferred transmission and a model calculation at the inferred temperature and density. Thus, we conclude that these potential sources of systematic error cannot account for the observed difference, increasing the likelihood of a real effect due to the high temperature and density conditions. However, because this is only a single experiment, we cannot make a firm conclusion. More experiments measuring the opacity and necessary calibrations are needed to assess the reproducibility and uncertainty of this result.

1. Introduction

Stars are a fundamental part of nearly all areas of astrophysics. Our understanding of their structure and evolution is foundational for understanding the systems in which they exist, from planetary systems to galaxies. Opacity is an important quantity for modeling stars, and over the past two decades, our ability to accurately calculate opacities at stellar interior conditions has come into question [1,2].

In 2005, a revision to the measured abundances in the Sun [3] led to the discovery that standard solar models no longer agreed with helioseismic measurements in several key quantities, one of which is the location of the solar convection zone boundary (CZB) [1]. One hypothesis that was put forward to potentially resolve this discrepancy

was that the opacity of matter in the vicinity of the solar CZB might be higher than what opacity models predicted. Experiments performed at the Z Machine measured the opacity of iron at conditions approaching the solar CZB conditions [2,4], and they found that as temperature and density were increased, models began to underpredict the measured opacity. This measurement has spurred much theoretical effort [5–17] that has attempted to explain the observed differences between models and measurement, but the reason for this discrepancy remains an open question. A complementary experiment was soon developed at the National Ignition Facility (NIF) to reproduce the measurements [18–20].

* Corresponding author.

E-mail address: dmayes@utexas.edu (D.C. Mayes).

<https://doi.org/10.1016/j.hedp.2025.101177>

Received 14 November 2024; Received in revised form 13 January 2025; Accepted 16 February 2025

Available online 27 February 2025

1574-1818/© 2025 The Authors. Published by Elsevier B.V. This is an open access article under the CC BY-NC-ND license (<http://creativecommons.org/licenses/by-nc-nd/4.0/>).

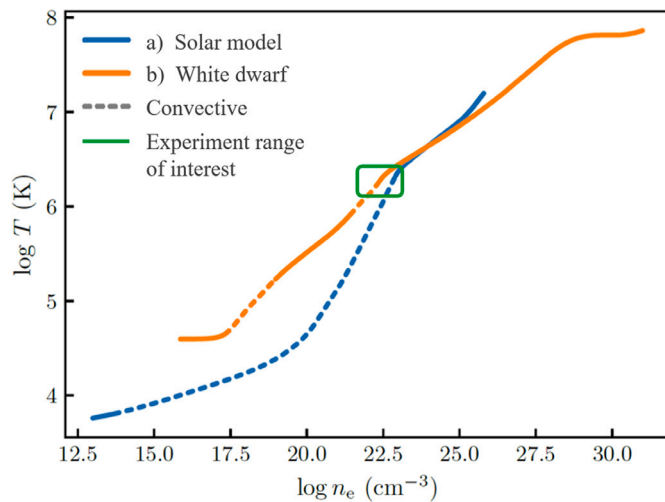


Fig. 1. Stellar interior tracks in the temperature-density plane for (a) a solar model and (b) a DQ white dwarf model. Dashed lines indicate convective regions in each model. The green square indicates the conditions of interest for the oxygen opacity experiments, overlapping with the convection zone base in both models.

The above work began with measuring iron for two reasons: (1) it is predicted to be the second largest contributor to the Rosseland mean opacity near the solar CZB, and (2) at these conditions, it produces a very complicated spectrum that is difficult to model, making it a likely candidate for inaccuracies. However, the largest contributor to the opacity at the CZB is predicted to be oxygen. At CZB conditions ($T_e \sim 190$ eV, $n_e \sim 1e23$ e $^-$ /cm 3), oxygen has 0 to 2 bound electrons, and it produces a relatively simple spectrum. One of the difficulties in calculating opacities at these conditions is how the model treats density effects, e.g. line broadening, continuum lowering, etc. This will be more important for a low-Z element like oxygen, in which the electrons are less tightly bound than iron, thus they can be more strongly perturbed at high densities. If the models are not handling density effects properly, then it could affect line widths, opacity windows, and the charge state distribution. Opacities have never been measured and benchmarked for CZB conditions, so the opacities that are presently used for modeling the Sun are only from a best-theory effort.

Additionally, oxygen opacity experiments can impact our understanding of white dwarf (WD) star physics. White dwarfs are stellar remnants from stars below about $10 M_{\odot}$, which accounts for around 97% of all stars. They have degenerate cores composed of a mixture of C and O, and their thin atmospheres generally contain H, He, or C, depending on their spectral type. Once a star becomes a WD, it is no longer capable of generating energy in the core, therefore, it only cools with time. This allows populations of WDs to be used as chronometers for measuring the ages of different morphological components of the Galaxy [21,22], revealing the age and assembly history of the Galaxy. Opacities are an important part of modeling the structure of WDs and how quickly they cool. Additionally, the DQ class of WDs, which has C and sometimes O in its atmosphere, has a convection zone boundary with very similar conditions to those of the Sun's CZB, as shown in Fig. 1. A discrepancy in the opacity of oxygen or carbon, which would be similarly affected by treatments for density effects, could affect predictions of when and where convection zones form in WDs, which will in turn affect WD cooling models and by extension, the inferred ages of their populations. In addition, some of the DQ WDs are thought to be the result of mergers that failed to become Type Ia supernovae [23]. Improving the accuracy of modeling these stars could help our understanding of this important phenomenon.

Experiments to measure the opacity of oxygen are being performed at both Z (starting in 2019) [24] and NIF (starting in 2021) using

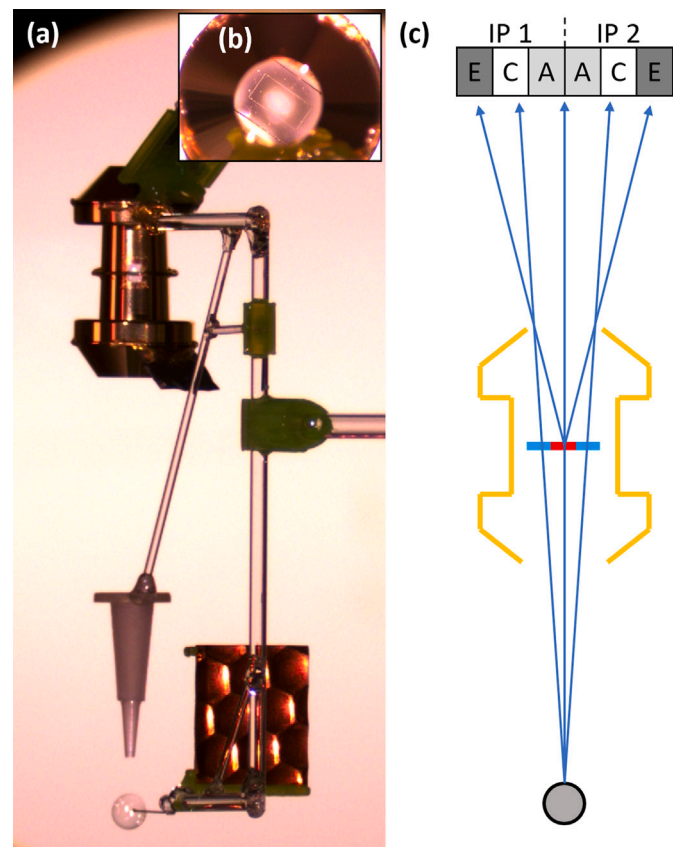


Fig. 2. (a) Laser target showing the hohlraum, capsule, and conical limiting aperture. The sample is at the center of the hohlraum. Diagnostic viewports are visible at the equator of the hohlraum. (b) Top down view of the sample in the hohlraum from the direction of the spectrometer. (c) Cartoon diagram (not to scale) demonstrating how the spectrometer setup produces three separate regions on each of the two image plate (IP) detectors. The radiation from the backlight (bottom) propagates through the heated sample plus tamper (red) and tamper-only (blue) toward the detectors (top). The regions are sample absorption “A”, backlight continuum “C”, and self-emission “E”.

similar methods to the experiments at each facility involving iron. This article provides an overview of the oxygen opacity experiments at NIF and then focuses on the investigation of three potential sources of systematic error in the experiments. Some of the findings here are also relevant to other experiments performed with the Opacity-on-NIF platform. Section 2 presents an overview of the platform and the specific differences necessary for fielding oxygen samples. This section also describes the diagnostics used and spectral data collected. Section 3 discusses the experimental results from tests to characterize three potential sources of systematic error due to background or data uniformity concerns. Finally, Section 4 concludes with a summary of the findings and some final remarks.

2. Experiment

The experimental setup is based upon the Opacity-on-NIF platform [19,20], which was originally developed for studying iron opacity at NIF. The laser target [25] (Fig. 2a) consists of four primary components: a hohlraum, a backlight capsule, a conical aperture, and the sample foil (Fig. 2b). Much of the setup is identical to that used for the iron experiments at NIF, but there are some important differences that we will discuss here.

The hohlraum is the “Apollo” style hohlraum [26]. It consists of two conical end caps connected in the middle by a tapered cylinder. At

each end is a laser entrance hole (LEH) that allows the laser to drive the hohlraum with 64 (up to 96) NIF beams. The hohlraum geometry shields the sample from directly viewing the laser spots. At the equator of the cylindrical section, there are two rectangular holes on opposite sides, which are used as diagnostic viewing windows. The sample foil is placed at the center of the hohlraum in the equatorial plane with its long edge toward the viewing windows.

The opacity sample consists of a small 1 mm \times 2 mm foil tamped with either 6 μm or 15 μm of CH plastic on top and bottom. The tamper thickness controls the speed of expansion, with a thicker tamper producing a higher density plasma. The tamper material extends out to the hohlraum wall on each side and is used to suspend the sample in the center of the hohlraum. The sample materials for these oxygen opacity experiments are either MgO, a bi-layer of MgO and SiO₂, or, more recently, SiO₂ co-sputtered with Mg. The first two sample types listed produce two different oxygen areal densities that differ by roughly a factor of two, i.e. $\sim 7.5 \times 10^{18}$ and $\sim 1.5 \times 10^{19}$ O/cm². The more recent co-sputtered samples allow independent adjustment of the O and Mg areal densities, which have been used to create even thicker samples containing up to $\sim 3 \times 10^{19}$ O/cm². Large areal densities of oxygen are required for a sufficient oxygen absorption signal at the relevant conditions, making the samples relatively thick. Varying the oxygen areal density allows for the use of Beer's Law to check the reproducibility in the measured opacity from samples of different optical thickness. Aside from providing oxygen-containing compounds with which to make samples, the magnesium and silicon can also be used to diagnose the temperature and density of the sample plasma spectroscopically. This can be used as a consistency check with the primary temperature and density diagnostics from DANTE and GXD; however, the spectroscopic method is not used in this article.

The backlight [27] is an empty spherical CH capsule placed ~ 30 mm below the sample. The capsule is driven by 96 NIF beams to create a short (~ 300 ps), bright, broadband source of X-rays to backlight the opacity sample. The conical aperture placed between the capsule and the hohlraum acts to limit the viewable size of the backlight source to ~ 400 μm . In the oxygen opacity platform, a detached cone is used in order to avoid the use of oxygen-containing glues. Typically, an attached-cone backlight has been used on other Opacity-on-NIF experiments.

2.1. Diagnostics

Multiple diagnostics are fielded during each experiment to characterize the sample and experiment performance. The primary diagnostics include an X-ray spectrometer, two DANTE instruments, and a time-gated pinhole imager.

The Opacity Spectrometer (OpSpec) [28] is the primary diagnostic for measuring the opacity. It employs two elliptically-bent X-ray crystals, typically potassium acid phthalate (KAP), to measure the photon energy resolved transmission through the opacity sample. This is accomplished by utilizing the point-projection geometry of the backlight radiation propagating through the sample and tamper toward the detector area (Fig. 2c). The angled sides of the hohlraum cylinder and asymmetric LEHs prevent the OpSpec from viewing any part of the hohlraum itself. The configuration produces three distinct regions on each of the two image plate (IP) detectors. The inner-most region "A" records the attenuated backlight signal resulting from absorption through the opacity sample plus tamper (red region inside the hohlraum). Moving outward, the next region "C" records the backlight continuum signal passing through the tamper-only areas (blue region inside the hohlraum) to each side of the sample material. Finally, the regions labeled "E" are blocked from seeing the backlight and only receive the signal from the sample and tamper self-emission. Fig. 3 shows each of these regions in image plate data from bottom to top, respectively. This data is discussed further in Section 2.2.

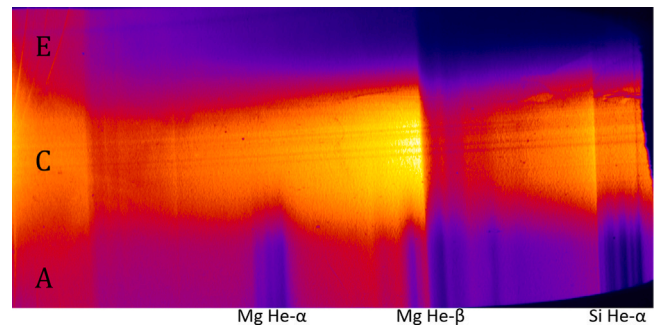


Fig. 3. Spectral image from shot N210615-1 with a MgO+SiO₂ sample. The regions are labeled sample absorption "A", backlight continuum "C", and self-emission "E". Photon energy increases toward the right.

Two DANTE [29,30] instruments are used in the experiment. DANTE-1 views the lower LEH and backlight capsule, which allows precise determination of the capsule flash time and, thus, when the sample probe time occurs. A dedicated capsule-only shot is required to characterize the temporal evolution, radiation temperature, and distribution of the backlight capsule emission alone [27]. DANTE-2 looks through a side window in the hohlraum and monitors the emission from the hohlraum's inner wall at a location near the opacity sample [31]. This measurement provides a method to infer the temperature in the sample. Simulations with LASNEX [32] are used to connect the hohlraum wall temperature with that of the sample. These simulations indicate that the sample temperature is ~ 4 eV higher than the DANTE-2 wall temperature measurements [31].

Lastly, the gated X-ray detector (GXD) [33,34] is a time-gated X-ray pinhole camera used to observe the sample edge-on through a second side window in the hohlraum as the sample expands [35]. The sample areal density is measured by General Atomic's Autoedge instrument [36] when the samples are manufactured. This is combined with the sample expansion thickness at probe time to give a measurement of the plasma ion density. To estimate the electron density, an estimate for the average ionization of the plasma is necessary. A rough estimate is obtained by assuming ionizations of 7 for O, 10 for Mg, and 12 for Si. Better estimates can be obtained from spectral synthesis codes, such as PrismSPECT [37], ATOMIC [38,39], or SCRAM [40,41].

2.2. Spectral data

Fig. 3 shows the spectral image data from shot N210615-1¹ with a bi-layer sample of MgO and SiO₂. The different spatial regions of the spectrum are labeled A, C, and E from bottom to top for sample absorption, backlight continuum, and self-emission, respectively. The vertical direction will be referred to as the spatial axis. Photon energy increases toward the right. In the absorption region, the He-like series of Mg and its Li-like satellites are visible near the center of the range. Toward the right end is the He- α line of Si and its satellite lines. Throughout the whole range, the bound-free absorption continuum from oxygen is present, and there is additional bound-free continuum absorption from Mg to the right of its He series. Spanning the whole spatial axis, at the left side and just right of center, are absorption edges of Na and Al from filters in the spectrometer. The edge-like feature toward the right side is a reflectivity feature seen in 2nd order from the KAP crystal.

The scanned IP data are first converted to units of photostimulated luminescence (PSL). A rotation is applied to make the backlight spatial

¹ The NIF shot notation begins with an "N", followed by two digits each for the year, month, and day. Finally, a daily sequence number is appended with a dash to indicate the shot's number within that day.

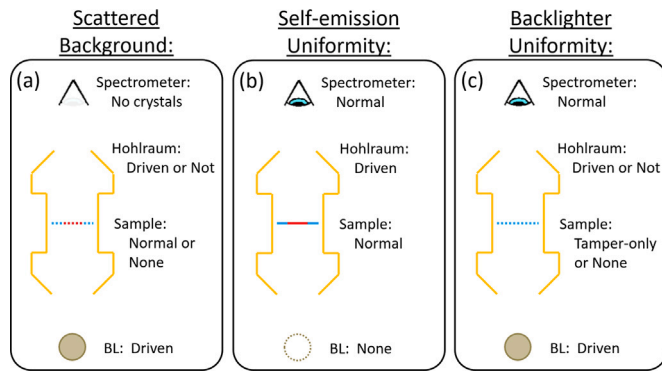


Fig. 4. Schematic diagrams of three experimental configurations to investigate potential sources of systematic error. In each case, each component is labeled “Normal” or “Driven” if it is the same as it would be in a standard shot. Other labels indicate some difference from the standard shot configuration. (a) shows a configuration that measures extra background signal due to scattered X-rays and fluorescence within the OpSpec. (b) shows a configuration that provides a measurement of the uniformity of the self-emission component across the spatial extent of the detector. (c) shows a configuration used to measure the uniformity of the backlight signal over the continuum and absorption regions.

peak horizontal. The filter and crystal edge features are then used to skew the image horizontally in order to align the photon energy axis along the spatial dimension. Finally, the wavelength calibration is performed with a dispersion model for OpSpec, again using the edge features as wavelength fiducials. A simple transmission spectrum can be extracted by taking horizontal lineouts from each of the three regions, subtracting out the emission contribution from both the continuum and absorption, and dividing these results as summarized by $T = (A - E)/(C - E)$.

In the process of computing the transmission, one can determine the relative contribution of 2nd and higher crystal orders to remove from the numerator and denominator by following the procedure outlined in Hobbs et al. [42]. Additionally, depending on the location of the lineouts relative to the boundaries between regions, a penumbral correction may need to be applied, as discussed in Dutra et al. [43]. For this study, the 2nd and higher order corrections are applied where relevant, but the penumbral correction is not because, for the data that are used, it was determined to be unnecessary.

The above process does not account for some potentially important sources of background and data uniformity concerns. First, it assumes that the emission component of the spectrum, as given by region E, captures all background sources that contribute to the measured signal and that these are uniform over the spatial axis. Second, it assumes that the isolated emission signal from region E is uniform over the spatial axis and is representative of the emission signals in both regions C and A. Third, it assumes that the backlight signal, as measured by region C, is uniform over the spatial axis and is representative of the unattenuated backlight intensity within the absorption region A. For each of these assumptions, dedicated experiments must be performed that isolate and measure each situation to verify whether or not the assumptions are valid. In the next section, we elaborate on our investigation into each of these issues and what has been found.

3. Background and data uniformity

There are multiple possible concerns regarding background or data uniformity that, unless properly accounted for, could render the transmission measurement inaccurate and produce systematic errors in the inferred opacity. Here, we discuss three of these possible concerns: scattered background, self-emission non-uniformity, and backlight non-uniformity.

In order to measure the effects of each of these concerns, we design “null” shots that isolate one potential concern and measure its spectrum. Fig. 4 shows schematics for three different types of experiments to provide information on each of these possible sources of systematic error.

The first of these, Fig. 4a, shows an experimental configuration that isolates one possible source for extra background signal in the data. There may be others. In this case, the primary difference from the normal experimental setup is that the diffracting element within the spectrometer is removed. The rest of the hardware, e.g. crystal mounts, detector boxes, filters, etc., are still included in the instrument. This configuration provides a measurement of any radiation reaching the detector that was either scattered within the instrument or the result of fluorescence of the instrument hardware.

In the second panel, Fig. 4b, the experiment is set up just like a standard experiment, except there is no backlight source. This allows for a measurement of the sample self-emission only, which can show how uniform this signal is over the spatial axis of the detector. This configuration would also capture any extra background signal that arises from this section of the platform when the hohlraum is driven.

The last panel, Fig. 4c, shows an experimental configuration for which the goal is to measure the uniformity of the backlight source spectrum over the detector plane. There are multiple options for what to do with the hohlraum and sample in this scenario. The version that we will focus on is one in which the hohlraum is empty and not driven by lasers. In this case, the hohlraum primarily acts as an aperture in the same way as it does in a standard experiment. Additionally, since the oxygen platform uses a cone collimator that is detached from the capsule, that will be the type used here.

The following subsections examine data from experiments with each of these configurations to assess the effect they have on an oxygen dataset. We proceed in step-wise fashion, beginning with the simplest version of the inferred transmission as a baseline, then applying each correction to the previous result in four steps: (1) 2nd order correction, (2) scattered background subtraction, (3) self-emission uniformity correction, and (4) backlight uniformity correction.

3.1. Baseline spectrum

In order to assess the effect of each of these background/uniformity concerns, we work with the spectral data from oxygen shot N220316-1, hereafter referred to as “S04”. This is a shot with a bi-layer sample of SiO₂ and MgO with 15 μm of tamper on both sides. DANTE and GXD infer electron temperature and density conditions of $T_e = 142 \pm 7$ eV and $n_e = (2.1 \pm 0.3) \times 10^{22}$ electrons/cm³, referred to as Anchor 1+ (i.e. lower temperature, higher density) following the system established in Bailey et al. 2015 [2]. In this particular shot data, information from both OpSpec IPs is combined to make the best inference of the transmission. The absorption lineout came from IP2, since that area of IP1 was severely cut off, making it the only option. The emission lineout came from IP1 because there was filter breakage evident in IP2, altering the signal there. In locations where there was no breakage, the emission signals from both IPs agreed well. Finally, the backlight continuum lineout also came from IP1, which had a higher signal than IP2. The lineout from IP1 was chosen because the distance between the A-C and C-E boundaries was found to be larger in IP1, meaning that the backlight signal was less likely to be artificially reduced in this IP due to blending from the neighboring A and E regions. Each of these lineouts is shown in Fig. 5a and were taken from locations where the spatial profiles became relatively flat, indicating that there was no significant blending from neighboring regions. Derivatives of the spatial profiles were used to confirm this result, as well as to find the aforementioned region boundaries. Consequently, a penumbral correction [43] is not necessary for these data.

Computing the transmission from these lineouts gives the black trace in Fig. 5b, which we take as our baseline transmission prior to applying any corrections that we find in the following investigation. Also

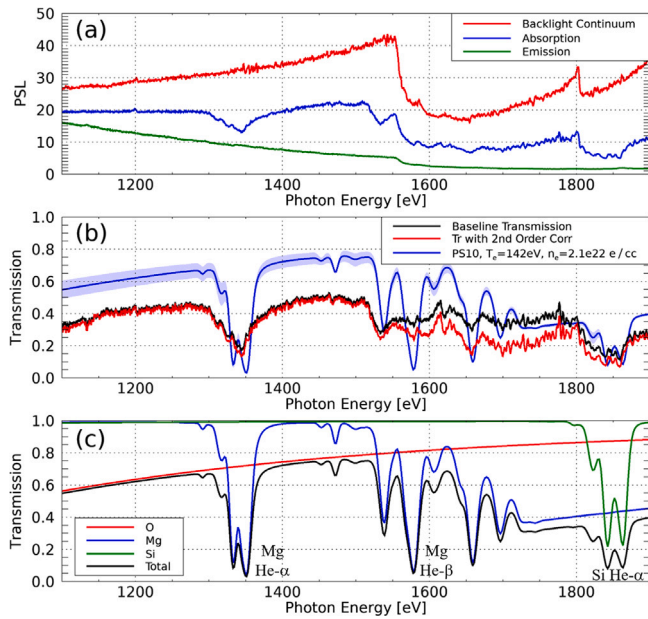


Fig. 5. (a) Lineouts from the backlight continuum (red), absorption (blue), and emission (green) taken from the N220316-1 shot data. (b) The resulting baseline transmission from the above lineouts before applying any corrections (black) and the transmission with the 2nd order correction [42] applied (red). In blue is a PrismSPECT 10.0.0 [37] model calculation at the inferred conditions with the shaded region showing the model variation, given the T_e and n_e uncertainties. (c) Breakdown of the model spectrum into elemental contributions showing that the continuum regions below 1500 eV are dominated by oxygen bound-free absorption.

shown in this panel is the transmission (red) resulting from applying the 2nd order correction according to Hobbs et al. 2024 [42]. In each of the following sections, the 2nd order correction must be applied to the corresponding corrected (A-E) and (C-E) spectra, which may alter its effect slightly, but this gives a sense of the level of effect the 2nd order correction has in general. This effect will be included in the final assessment of the total effect of the set of corrections as compared with the baseline transmission (black). Finally, also shown in panel b of this figure is a calculated transmission (blue) from PrismSPECT 10.0.0 [37] at the inferred conditions. The shaded region surrounding the line shows the extent of the variation due to the T_e and n_e uncertainties. The calculated spectrum is broken down into its elemental contributions in Fig. 5c, showing that the continuum regions below 1500 eV are expected to be dominated by oxygen bound-free absorption.

3.2. Scattered background

The goal of a scattered background null shot (Fig. 4a) is to measure the spatial distribution of this signal on the detector plane and to be able to subtract it from other shot data as a correction. Image data from oxygen shot S04 is shown in Fig. 6a, and the data from scattered background null shot N210922-3 is shown in Fig. 6b. In order to accomplish this goal, the null data image must be aligned and often scaled to match with the background present in the standard data image. Once this procedure is complete, the scattered background can be subtracted [44]. Then one can continue with the steps that are necessary to obtain the transmission.

The result from applying this correction to the S04 shot data is shown in Fig. 6c as the red trace. The overall effect is relatively small and primarily affects the lower photon energy region. However, the effect on the inferred opacity in this area is up to 10%–15% in this case.

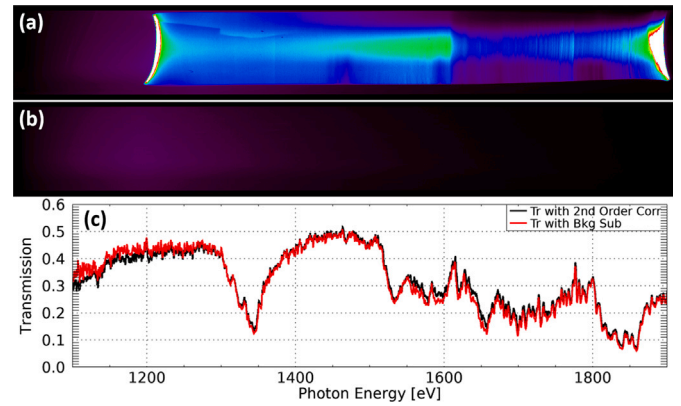


Fig. 6. The top image (a) shows standard oxygen data from shot N220316-1. The lower image (b) shows data from shot N210922-3, a scattered background null shot. The purple region of this image is the scattered background signal, which can also be seen underneath the standard data. (c) Shows the effect of subtracting the background image from the data prior to computing the transmission. The red trace shows this result compared with the 2nd order corrected version from Fig. 5 shown here in black.

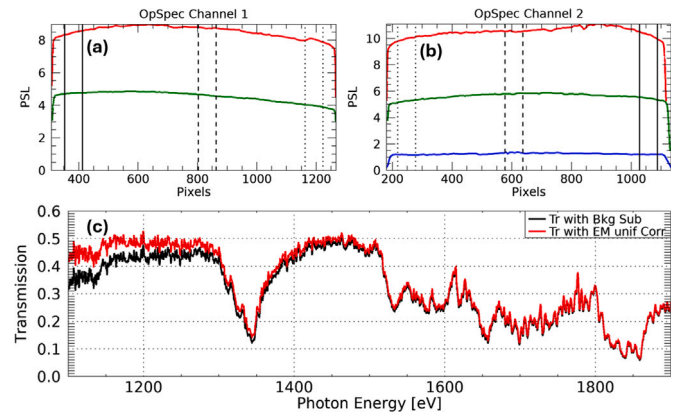


Fig. 7. (a) and (b) show spatial profiles from OpSpec IPs 1 and 2 from shot N230801-3. The red, green, and blue sample profiles correspond to lower, middle, and higher photon energy areas of the spectral image. Vertical black lines indicate the positions of the E (solid), C (dashed), and A (dotted) lineout boundaries. (c) shows the result (red) of scaling the E region lineout prior to subtracting it from the C and A lineouts. This is compared with the previous result (black) from Fig. 6.

3.3. Self-emission uniformity

There are two objectives of measuring the self-emission spectrum alone (Fig. 4b): (1) Assess whether the signal is uniform (i.e. flat) over the spatial dimension or measure how it varies. (2) If it is not uniform, this measurement gives a quantitative way to correct for the non-uniformity by scaling the emission region according to how it is found to vary as a function of position.

To assess this, we examined spatial profiles from emission-only null shot N230801-3 (S09). A sample of these profiles are shown in Fig. 7 panels a and b. The emission signal is strongest at low photon energies (red) and weakens toward higher photon energies (green then blue). These show that there is non-uniformity along the spatial direction in the emission data, with a depression toward the central axis of the instrument. Similar profile shapes have been seen in other self-emission shots with different sample types but with the same laser drive type. This may suggest the existence of attenuating material on axis in the hohlraum, but this hypothesis has not been verified. To assess the level of effect this non-uniformity may have on the transmission, the relative locations of the spectral lineouts from S04 were overlaid onto to these profiles, and since there are no reference points in this direction these were centered between the edges. The values within

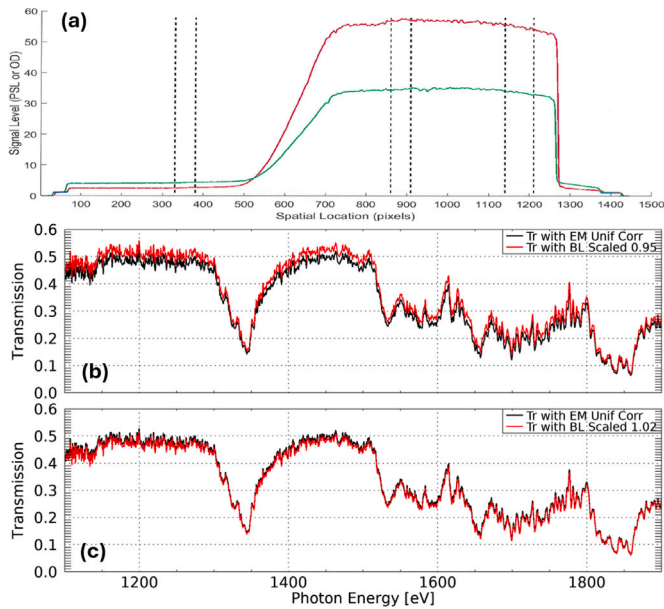


Fig. 8. (a) Spatial profiles from two different positions in the image data from detached-cone backlight null shot N230906-1. Vertical dotted lines indicate the locations of E, C, and A lineout regions (left to right) based on those from S04 positioned relative to the E-C boundary location (i.e. center of slope). (b) and (c) show the results (red) of scaling the backlight continuum spectrum by the minimum and maximum seen in the null shot’s “transmission”. The black trace in each is the previous result from Fig. 7.

the backlight (dashed lines) and absorption (dotted lines) regions were compared with the emission region (solid lines). The backlight area was found to be an average of 1.04 times higher and the absorption region was on average 0.94 lower than the emission region. To see the effect on the transmission, we scaled the emission spectrum from S04 by these average values to estimate the emission level to subtract from the backlight and absorption spectra. The result of this is shown in Fig. 7c as the red trace compared with the result of the previous section in black. The effect is stronger at lower photon energies where the emission signal is strongest, but the effect becomes small above 1400 eV. The effect on the inferred opacity near the edge of the plot surpasses 20% and becomes less than 5% above 1400 eV.

3.4. Backlighter uniformity

The goals of measuring the backlight uniformity are similar to those of the self-emission uniformity. (1) Assess whether the signal is uniform (i.e. flat) over the spatial dimension in the C and A regions or measure how it varies. (2) If it is not uniform, this measurement could give a quantitative way to correct for the non-uniformity by scaling the backlight region according to how it is found to vary as a function of position in the absorption region.

Data from null shot N230906-1, which had a backlight capsule and an empty, undriven hohlraum was used to assess the backlight uniformity. Fig. 8a shows a sample of spatial profiles from this shot. The vertical dashed lines show the locations of lineouts for the E (left), C (middle), and A (right) regions based on the relative locations of the lineouts in S04. These were located in this data relative to the midpoint of the slope between the E and C regions. From these lineouts, the “transmission” was calculated in the same way as for regular data. This showed variations ranging from 0.95 to 1.02. Given that this is a single shot and there is no clear reason for the photon energy dependence of this transmission curve, these values were taken to represent the extent of the effect this backlight non-uniformity could have. For each of these values, the emission-subtracted backlight spectrum from S04 is scaled by that value to give an estimate for the backlight level in the

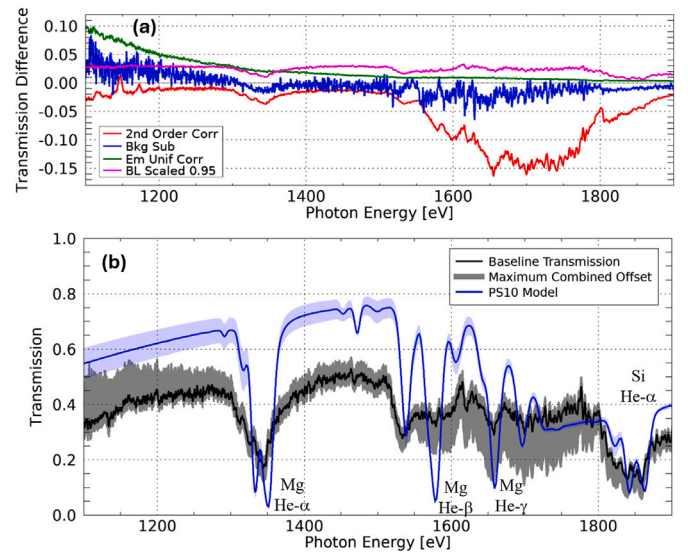


Fig. 9. (a) Plot with each difference in transmission resulting from the four concerns discussed: 2nd order correction (red), scattered background subtraction (blue), emission uniformity correction (green), and backlight uniformity correction (magenta). (b) Plot showing the maximum combined effect of the “corrections” investigated here. The black line is the original baseline spectrum from S04. The gray shaded region shows the combined offset upward and downward from the baseline spectrum obtained when taking each of the four concerns into account. The blue trace with shaded region is the same PrISM SPECT model as in Fig. 5b.

absorption region. This results in scaling the transmission slightly up or down, respectively as seen in Fig. 8 panels b and c. Here, the red traces are each result and these are compared with the result from the previous section in black. The effect on the inferred opacity in the area dominated by oxygen bound-free absorption ranges from 3% to 8%.

4. Discussion

As described in the introduction, one of the main motivations for these experiments was the hypothesis that higher than predicted opacities of iron and oxygen at conditions in the solar interior could resolve the discrepancy between the predicted and observed location of the solar convection zone boundary. Indeed, the measurements of the opacity of iron on Z show higher opacities than predicted, and now the measurements of oxygen on NIF seem to show higher opacities as well. However, in both cases the reason for higher opacities is still an open question, and the experimental results must be rigorously validated.

The primary goal of this investigation was to determine whether any of the above-described potential sources of background and data non-uniformity could account for the large discrepancy initially observed between the oxygen data recorded for Anchor 1+ conditions and model calculations at the measured conditions. Fig. 9a shows the differences from the previous transmission as we went sequentially through each concern. Fig. 9b shows the maximum combined effect that we obtained when taking these concerns into account. The gray shaded region surrounding the black baseline transmission combines all upward and downward offsets found during the course of this exercise. This is not an uncertainty, rather it is intended to show the maximum combined offset to the original transmission in either direction due to these concerns. The result is that none of these concerns alone or combined seem to be enough to account for the observed difference between the model and data.

Converting the transmission curves of Fig. 9b to opacities shows that in the area dominated by the oxygen bound-free absorption the measured opacity is about a factor of 1.5 to 2 higher than the predicted opacity. One possible explanation for this is that the predicted ion

balance is wrong. According to the PrismSPECT model, the oxygen ions at these conditions are dominated by hydrogen-like (i.e. bare ions 32%, H-like 54%, and He-like 13%). If the oxygen ion balance were shifted more toward helium-like, the predicted opacity could be increased to remove the discrepancy. Some of the theoretical efforts mentioned earlier [5–17] predict that as electron density increases, there is a shift to lower ionization states than is predicted by models like PrismSPECT. However, it is unclear whether or not the magnitude of shift predicted would be enough to match the experimental results. Efforts are underway to extend the spectral range of the spectrometer so that the ion balance of the plasma can be measured more directly.

The findings of this investigation strengthens the viewpoint that these data might be indicative of problems with opacity models as one enters into this regime of conditions; however, there is more work to be done to evaluate the accuracy of these measurements before making such a bold claim. This investigation only included a single shot for the oxygen transmission measurement, as well as for each calibration measurement. This small number of measurements does not allow an assessment of reproducibility for the inferred transmission or any of these potential systematic concerns. Thus, the true uncertainties for these measurements are still unknown. Additional repeated shots of these types, especially the oxygen transmission measurement, are necessary for such an assessment. Additionally, there may be other potential sources of systematic error than what has been covered here. Lastly, we have not addressed what is causing the non-uniformity of the emission and backlight signals. Understanding the cause of this behavior was outside the scope of this investigation, since the goal was to simply assess the level of the effect on the transmission that these concerns might have from an ideal situation. However, understanding the cause could lead to a different interpretation of how these issues should be addressed.

CRediT authorship contribution statement

D.C. Mayes: Writing – original draft, Visualization, Methodology, Investigation, Formal analysis, Data curation, Conceptualization. **B.A. Hobbs:** Software, Methodology, Formal analysis, Conceptualization. **R.F. Heeter:** Supervision, Methodology, Investigation, Data curation, Conceptualization. **T.S. Perry:** Writing – review & editing, Supervision, Investigation, Conceptualization. **H.M. Johns:** Supervision, Resources, Investigation, Data curation. **Y.P. Opachich:** Resources, Investigation, Formal analysis. **M. Hohenberger:** Investigation, Formal analysis, Data curation. **P.A. Bradley:** Writing – review & editing, Software, Data curation. **E.C. Dutra:** Resources, Methodology. **C.J. Fontes:** Writing – review & editing, Software. **E. Gallardo-Diaz:** Writing – review & editing, Methodology. **M.H. Montgomery:** Supervision, Funding acquisition. **H.F. Robey:** Data curation. **M.S. Wallace:** Writing – review & editing, Resources. **D.E. Winget:** Supervision, Funding acquisition.

Declaration of competing interest

The authors declare that they have no known competing financial interests or personal relationships that could have appeared to influence the work reported in this paper.

Acknowledgments

The authors would like thank the Z opacity team, J. E. Bailey, T. Nagayama, and G. P. Loisel, for their contributions to experimental design strategies, discussions, and freely sharing ideas. Additionally, we thank the Z opacity team and P. B. Cho for reviewing this manuscript and providing useful suggestions.

This work was supported by the Wootton Center for Astrophysical Plasma Properties under the National Nuclear Security Administration, Stewardship Science Academic Alliances award number DE-NA0004149. Experimental time was provided by the NIF Discovery

Science Program of Lawrence Livermore National Laboratory. Additionally, work was performed under the auspices of the U.S. Department of Energy (DOE) by Lawrence Livermore National Laboratory under Contract No. DEAC52-07NA27344; Los Alamos National Laboratory under Contract No. 89233218CNA000001; and the Nevada National Security Site, Mission Support, and Test Services under Contract No. DE-NA0003624 with the U.S. DOE and supported by the National Nuclear Security Administration, Office of Defense Programs.

Data availability

Data will be made available on request.

References

- [1] S. Basu, H.M. Antia, Helioseismology and solar abundances, *Phys. Rep.* 457 (5–6) (2008) 217–283, <http://dx.doi.org/10.1016/j.physrep.2007.12.002>.
- [2] J.E. Bailey, T. Nagayama, G.P. Loisel, G.A. Rochau, C. Blancard, J. Colgan, P. Cosse, G. Faussurier, C.J. Fontes, F. Gilleron, I. Golovkin, S.B. Hansen, C.A. Iglesias, D.P. Kilcrease, J.J. MacFarlane, R.C. Mancini, S.N. Nahar, C. Orban, J.-C. Pain, A.K. Pradhan, M. Sherrill, B.G. Wilson, A higher-than-predicted measurement of iron opacity at solar interior temperatures, *Nature* 517 (7532) (2015) 56–59, <http://dx.doi.org/10.1038/nature14048>.
- [3] M. Asplund, N. Grevesse, A.J. Sauval, C.A. Prieto, R. Blomme, Line formation in solar granulation, *Astron. Astrophys.* 431 (2) (2005) 693–705, <http://dx.doi.org/10.1051/0004-6361:20041951>.
- [4] T. Nagayama, J. Bailey, G. Loisel, G. Dunham, G. Rochau, C. Blancard, J. Colgan, P. Cossé, G. Faussurier, C. Fontes, F. Gilleron, S. Hansen, C. Iglesias, I. Golovkin, D. Kilcrease, J. MacFarlane, R. Mancini, R. More, C. Orban, J.-C. Pain, M. Sherrill, B. Wilson, Systematic study of l-shell opacity at stellar interior temperatures, *Phys. Rev. Lett.* 122 (23) (2019) 235001, <http://dx.doi.org/10.1103/physrevlett.122.235001>.
- [5] R.A. Baggott, S.J. Rose, S.P.D. Mangles, Calculating opacity in hot, dense matter using second-order electron-photon and two-photon transitions to approximate line broadening, *Phys. Rev. Lett.* 125 (14) (2020) 145002, <http://dx.doi.org/10.1103/physrevlett.125.145002>.
- [6] N.M. Gill, C.J. Fontes, C.E. Starrett, Time-dependent density functional theory applied to average atom opacity, *Phys. Rev. E* 103 (4) (2021) 043206, <http://dx.doi.org/10.1103/physreve.103.043206>.
- [7] N.M. Gill, C.J. Fontes, C.E. Starrett, A superconfiguration calculation of opacity with consistent bound and continuum electron treatments using green's functions, *J. Phys. B: At. Mol. Opt. Phys.* 56 (1) (2023) 015001, <http://dx.doi.org/10.1088/1361-6455/acad9>.
- [8] T.A. Gomez, T. Nagayama, P.B. Cho, M.C. Zammit, C.J. Fontes, D.P. Kilcrease, I. Bray, I. Hubeny, B.H. Dunlap, M.H. Montgomery, D.E. Winget, All-order full-Coulomb quantum spectral line-shape calculations, *Phys. Rev. Lett.* 127 (23) (2021) 235001, <http://dx.doi.org/10.1103/physrevlett.127.235001>.
- [9] V.V. Karasiev, S.X. Hu, N.R. Shaffer, G. Miloshevsky, First-principles study of L-shell iron and chromium opacity at stellar interior temperatures, *Phys. Rev. E* 106 (6) (2022) 065202, <http://dx.doi.org/10.1103/physreve.106.065202>.
- [10] M. Krief, A. Feigel, D. Gazit, Line broadening and the solar opacity problem, *Astrophys. J.* 824 (2) (2016) 98, <http://dx.doi.org/10.3847/0004-637x/824/2/98>.
- [11] M.K.G. Kruse, C.A. Iglesias, Two-photon absorption framework for plasma transmission experiments, *High Energy Density Phys.* 31 (2019) 38–46, <http://dx.doi.org/10.1016/j.hedp.2019.02.004>.
- [12] R.M. More, S.B. Hansen, T. Nagayama, Opacity from two-photon processes, *High Energy Density Phys.* 24 (2017) 44–49, <http://dx.doi.org/10.1016/j.hedp.2017.07.003>.
- [13] J.-C. Pain, F. Gilleron, M. Comet, Detailed opacity calculations for astrophysical applications, *Atoms* 5 (2) (2017) 22, <http://dx.doi.org/10.3390/atoms502022>.
- [14] N.R. Shaffer, C.E. Starrett, Dense plasma opacity via the multiple-scattering method, *Phys. Rev. E* 105 (1) (2022) 015203, <http://dx.doi.org/10.1103/physreve.105.015203>.
- [15] C.E. Starrett, N. Shaffer, Multiple scattering theory for dense plasmas, *Phys. Rev. E* 102 (4) (2020) 043211, <http://dx.doi.org/10.1103/physreve.102.043211>.
- [16] J. Zeng, C. Gao, P. Liu, Y. Li, C. Meng, Y. Hou, D. Kang, J. Yuan, Electron localization enhanced photon absorption for the missing opacity in solar interior, *Sci. China Phys. Mech. Astron.* 65 (3) (2021) <http://dx.doi.org/10.1007/s11433-021-1812-1>.
- [17] J. Zeng, Y. Li, Y. Hou, J. Yuan, Nonideal effect of free electrons on ionization equilibrium and radiative property in dense plasmas, *Phys. Rev. E* 107 (3) (2023) 033201, <http://dx.doi.org/10.1103/physreve.107.033201>.

- [18] T.S. Perry, R.F. Heeter, Y.P. Opachich, P.W. Ross, J.L. Kline, K.A. Flippo, M.E. Sherrill, E.S. Dodd, B.G. DeVolder, T. Cardenas, T.N. Archuleta, R.S. Craxton, R. Zhang, P.W. McKenty, E.M. Garcia, E.J. Huffman, J.A. King, M.F. Ahmed, J.A. Emig, S.L. Ayers, M.A. Barrios, M.J. May, M.B. Schneider, D.A. Liedahl, B.G. Wilson, T.J. Urbatsch, C.A. Iglesias, J.E. Bailey, G.A. Rochau, Replicating the z iron opacity experiments on the NIF, *High Energy Density Phys.* 23 (2017) 223–227, <http://dx.doi.org/10.1016/j.hedp.2017.05.006>.
- [19] R.F. Heeter, J.E. Bailey, R.S. Craxton, B.G. DeVolder, E.S. Dodd, E.M. Garcia, E.J. Huffman, C.A. Iglesias, J.A. King, J.L. Kline, D.A. Liedahl, P.W. McKenty, Y.P. Opachich, G.A. Rochau, P.W. Ross, M.B. Schneider, M.E. Sherrill, B.G. Wilson, R. Zhang, T.S. Perry, Conceptual design of initial opacity experiments on the national ignition facility, *J. Plasma Phys.* 83 (1) (2017) <http://dx.doi.org/10.1017/s0022377816001173>.
- [20] R. Heeter, T. Perry, H. Johns, K. Opachich, M. Ahmed, J. Emig, J. Holder, C. Iglesias, D. Liedahl, R. London, M. Martin, N. Thompson, B. Wilson, T. Archuleta, T. Cardenas, E. Dodd, M. Douglas, K. Flippo, C. Fontes, J. Kline, L. Kot, N. Krasheninnikova, M. Sherrill, T. Urbatsch, E. Huffman, J. King, R. Knight, J. Bailey, G. Rochau, Iron X-ray transmission at temperature near 150 eV using the national ignition facility: First measurements and paths to uncertainty reduction, *Atoms* 6 (4) (2018) 57, <http://dx.doi.org/10.3390/atoms6040057>.
- [21] D.E. Winget, C.J. Hansen, J. Liebert, H.M.V. Horn, G. Fontaine, R.E. Nather, S.O. Kepler, D.Q. Lamb, An independent method for determining the age of the universe, *Astrophys. J.* 315 (1987) L77, <http://dx.doi.org/10.1086/184864>.
- [22] D. Saumon, S. Blouin, P.-E. Tremblay, Current challenges in the physics of white dwarf stars, *Phys. Rep.* 988 (2022) 1–63, <http://dx.doi.org/10.1016/j.physrep.2022.09.001>.
- [23] B.H. Dunlap, *The origin of carbon-atmosphere white dwarfs with implications for Type Ia supernovae* (Ph.D. thesis), University of North Carolina at Chapel Hill, 2015.
- [24] J. Bailey, Oxygen opacity experiments for stellar interiors, in: *62nd Annual Meeting of the American Physical Society Division of Plasma Physics*, 2020.
- [25] T. Cardenas, D.W. Schmidt, E.S. Dodd, T.S. Perry, D. Capelli, T. Quintana, J.A. Oertel, D. Peterson, E. Giraldez, R.F. Heeter, Design and fabrication of opacity targets for the national ignition facility, *Fusion Sci. Technol.* 73 (3) (2017) 458–466, <http://dx.doi.org/10.1080/15361055.2017.1389559>.
- [26] E.S. Dodd, B.G. DeVolder, M.E. Martin, N.S. Krasheninnikova, I.L. Tregillis, T.S. Perry, R.F. Heeter, Y.P. Opachich, A.S. Moore, J.L. Kline, H.M. Johns, D.A. Liedahl, T. Cardenas, R.E. Olson, B.H. Wilde, T.J. Urbatsch, Hohlräum modeling for opacity experiments on the National Ignition Facility, *Phys. Plasmas* 25 (6) (2018) 063301, <http://dx.doi.org/10.1063/1.5026285>.
- [27] Y.P. Opachich, R.F. Heeter, M.A. Barrios, E.M. Garcia, R.S. Craxton, J.A. King, D.A. Liedahl, P.W. McKenty, M.B. Schneider, M.J. May, R. Zhang, P.W. Ross, J.L. Kline, A.S. Moore, J.L. Weaver, K.A. Flippo, T.S. Perry, Capsule implosions for continuum x-ray backlighting of opacity samples at the National Ignition Facility, *Phys. Plasmas* 24 (6) (2017) 063301, <http://dx.doi.org/10.1063/1.4985076>.
- [28] M.S. Wallace, R.F. Heeter, R.A. Knight, A.M. Durand, J.M. Heinmiller, R.B. Lara, D.A. Max, E.C. Dutra, E.J. Huffman, J. Ayers, J.A. Emig, T.N. Archuleta, T.J. Urbatsch, T.S. Perry, Upgrades and redesign of the National Ignition Facility's soft x-ray opacity spectrometer (OpSpec), *Rev. Sci. Instrum.* 92 (3) (2021) 035108, <http://dx.doi.org/10.1063/5.0043517>.
- [29] E.L. Dewald, K.M. Campbell, R.E. Turner, J.P. Holder, O.L. Landen, S.H. Glenzer, R.L. Kauffman, L.J. Suter, M. Landon, M. Rhodes, D. Lee, Dante soft x-ray power diagnostic for National Ignition Facility, *Rev. Sci. Instrum.* 75 (10) (2004) 3759–3761, <http://dx.doi.org/10.1063/1.1788872>.
- [30] J.L. Kline, K. Widmann, A. Warrick, R.E. Olson, C.A. Thomas, A.S. Moore, L.J. Suter, O. Landen, D. Callahan, S. Azevedo, J. Liebman, S.H. Glenzer, A. Conder, S.N. Dixit, P. Torres, V. Tran, E.L. Dewald, J. Kamperschroer, L.J. Atherton, R. Beeler, L. Berzins, J. Celeste, C. Haynam, W. Hsing, D. Larson, B.J. MacGowan, D. Hinkel, D. Kalantar, R. Kauffman, J. Kilkenny, N. Meezan, M.D. Rosen, M. Schneider, E.A. Williams, S. Vernon, R.J. Wallace, B.V. Wonerghem, B.K. Young, The first measurements of soft x-ray flux from ignition scale Hohlräume at the National Ignition Facility using DANTE (invited), *Rev. Sci. Instrum.* 81 (10) (2010) 10E321, <http://dx.doi.org/10.1063/1.3491032>.
- [31] Y.P. Opachich, E.S. Dodd, R.F. Heeter, C.D. Harris, H.M. Johns, J.L. Kline, N.S. Krasheninnikova, M.J. May, A.S. Moore, M.S. Rubery, M.B. Schneider, T.J. Urbatsch, K. Widmann, T.S. Perry, DANTE as a primary temperature diagnostic for the NIF iron opacity campaign, *Rev. Sci. Instrum.* 92 (3) (2021) 033519, <http://dx.doi.org/10.1063/5.0040972>.
- [32] G.B. Zimmerman, W.L. Krueer, *The LASNEX Code for Inertial Confinement Fusion, Comments Plasma Phys. Control. Thermonucl. Fusion* 2 (1975) 85.
- [33] J.A. Oertel, R. Aragonéz, T. Archuleta, C. Barnes, L. Casper, V. Fotherley, T. Heinrichs, R. King, D. Landers, F. Lopez, P. Sanchez, G. Sandoval, L. Schrank, P. Walsh, P. Bell, M. Brown, R. Costa, J. Holder, S. Montelongo, N. Pederson, Gated x-ray detector for the National Ignition Facility, *Rev. Sci. Instrum.* 77 (10) (2006) 10E308, <http://dx.doi.org/10.1063/1.2227439>.
- [34] L.R. Benedetti, P.M. Bell, D.K. Bradley, C.G. Brown, S.M. Glenn, R. Heeter, J.P. Holder, N. Izumi, S.F. Khan, G. Lacaille, N. Simanovskaia, V.A. Smalyuk, R. Thomas, Crosstalk in x-ray framing cameras: Effect on voltage, gain, and timing (invited), *Rev. Sci. Instrum.* 83 (10) (2012) 10E135, <http://dx.doi.org/10.1063/1.4740524>.
- [35] Y.P. Opachich, R.F. Heeter, H.M. Johns, E.S. Dodd, J.L. Kline, N.S. Krasheninnikova, D.C. Mayes, M.H. Montgomery, D.E. Winget, T.J. Urbatsch, T.S. Perry, Density measurements for the National Ignition Facility (NIF) opacity platform, *Rev. Sci. Instrum.* 93 (11) (2022) 113515, <http://dx.doi.org/10.1063/5.0099764>.
- [36] H. Huang, K. Sequoia, M. Yamaguchi, K.J. Boehm, K. Engelhorn, J. Walker, F. Elsner, J. Tomlin, M. Farrell, C.J. Fontes, J.P. Colgan, Improved x-ray mass attenuation coefficient (opacity) measurements for Fe, Ni and Au, *J. Phys. B: At. Mol. Opt. Phys.* 54 (11) (2021) 115003, <http://dx.doi.org/10.1088/1361-6455/abf01c>.
- [37] J.J. MacFarlane, I.E. Golovkin, P.R. Woodruff, D.R. Welch, B.V. Oliver, T.A. Mehlhorn, R.B. Campbell, Simulation of the ionization dynamics of aluminum irradiated by intense short-pulse lasers, in: *Proceedings of Inertial Fusion and Science Applications 2003, American Nuclear Society, La Grange Park, IL, 2004*.
- [38] P. Hakel, M.E. Sherrill, S. Mazevet, J. Abdallah, J. Colgan, D.P. Kilcrease, N.H. Magee, C.J. Fontes, H.L. Zhang, The new Los Alamos opacity code ATOMIC, *J. Quant. Spectrosc. Radiat. Transfer* 99 (1–3) (2006) 265–271, <http://dx.doi.org/10.1016/j.jqsrt.2005.04.007>.
- [39] C.J. Fontes, H.L. Zhang, J.A. Jr., R.E.H. Clark, D.P. Kilcrease, J. Colgan, R.T. Cunningham, P. Hakel, N.H. Magee, M.E. Sherrill, The Los Alamos suite of relativistic atomic physics codes, *J. Phys. B: At. Mol. Opt. Phys.* 48 (14) (2015) 144014, <http://dx.doi.org/10.1088/0953-4075/48/14/144014>.
- [40] S.B. Hansen, J. Bauche, C. Bauche-Arnoult, M.F. Gu, Hybrid atomic models for spectroscopic plasma diagnostics, *High Energy Density Phys.* 3 (1–2) (2007) 109–114, <http://dx.doi.org/10.1016/j.hedp.2007.02.032>.
- [41] S. Hansen, Configuration interaction in statistically complete hybrid-structure atomic models, *Can. J. Phys.* 89 (5) (2011) 633–638, <http://dx.doi.org/10.1139/p11-006>.
- [42] B.A. Hobbs, D.C. Mayes, R.F. Heeter, P.A. Bradley, E.C. Dutra, C.J. Fontes, E. Gallardo-Diaz, M. Hohenberger, H.M. Johns, Y.P. Opachich, H.F. Robey, S. Stoupin, M.S. Wallace, L.G. Webster, M.H. Montgomery, T.S. Perry, D.E. Winget, Development of improved higher-order correction for the NIF opacity spectrometer, *Rev. Sci. Instrum.* 95 (8) (2024) <http://dx.doi.org/10.1063/5.0219317>.
- [43] E.C. Dutra, J. Emig, C.J. Fontes, R.F. Heeter, Y.P. Opachich, H.F. Robey, M.S. Wallace, T.S. Perry, 2nd and 3rd order spectral energy corrections with penumbral de-blurring methodology for opacity platform used on the National Ignition Facility, *Rev. Sci. Instrum.* 93 (11) (2022) 113527, <http://dx.doi.org/10.1063/5.0101833>.
- [44] E. Gallardo-Diaz, 2023, *Personal communication*.